RSC Advances

PAPER

View Article Online
View Journal | View Issue

Cite this: *RSC Adv.*, 2023, **13**, 29061

A hyperthermia-enhanced nanocatalyst based on asymmetric Au@polypyrrole for synergistic cancer Fenton/photothermal therapy†

Xixi Wu,[a] Huazhen Liang,[c] Chaoming Li,[c] Duanyang Zhou[d] and Rui Liu *[b]

The specific tumor microenvironment is a conducive breeding ground for malignant tumors, favoring their survival, rapid proliferation, and metastasis, which is also an inevitable obstacle to tumor treatment, particularly for catalytic therapy. To address this issue, a hyperthermia-enhanced nanocatalyst (AuP@MnO_2) consisting of an asymmetric Au@polypyrrole core and a MnO_2 shell is constructed for synergistic cancer Fenton/photothermal therapy. In an ultra-short reaction time (15 min), the innovative introduction of a new oxidizer, tetrachloroauric acid trihydrate, not only successfully initiates the oxidative polymerization of pyrrole monomer while reducing itself to cubic Au, but also accelerates the polymerization process by supplying protic acid. After MnO_2 coating, AuP@MnO_2 catalyzes the conversion of antioxidant GSH and excess H_2O_2 into GSSG and $^{\bullet}OH$ through Mn^{2+}/Mn^{4+} ion couples, leading to oxidative damage of tumor cells. More importantly, after 1064 nm laser irradiation, more extreme oxidative imbalance and cell death are demonstrated in this work under the combined effect of photothermal and catalytic therapy, with insignificant toxicity to normal cells. This work develops an efficient one-step synthesis method of asymmetric Au@polypyrrole and provides constructive insight into its oxidative stress-based antitumor treatment.

Received 16th July 2023
Accepted 18th September 2023

DOI: 10.1039/d3ra04779b

rsc.li/rsc-advances

1. Introduction

Catalytic nanomedicine, which employs biocompatible catalysts to catalyze specific reactions *in situ* to produce anticancer therapeutic substances in the tumor regions, has attracted increasing attention due to its unique advantages including noninvasiveness, spatiotemporal controllability, catalytic specificity, and high efficiency.[1–4] Thereinto, one of the most commonly used catalytic strategies is the Fenton or Fenton-like reaction, in which catalysts containing Fe^{2+}, Cu^{+}, and Mn^{2+} react with excess hydrogen peroxide (H_2O_2) in the tumor microenvironment to produce hydroxyl radicals ($^{\bullet}OH$) that can kill cancer cells.[5–8] However, the efficiency of this catalytic reaction is dependent on several factors such as catalyst species, H_2O_2 concentration, reaction temperature, *etc.*[9–11] In addition, the antioxidant glutathione (GSH), which is abundant in tumor cells, will be activated to maintain cellular oxidative homeostasis by depleting generated $^{\bullet}OH$.[12,13] To improve catalytic efficiency and achieve tumor clearance, high concentrations of catalysts are often administered to increase $^{\bullet}OH$ production, but doing so also raises the possibility of negative health effects due to toxic spillover.[14,15] Alternatively, raising the local temperature of the tumor using exogenous laser can accelerate the Fenton reaction, even at low catalyst concentrations.

In recent decades, the photothermal transducing agents (PTAs) that absorb and convert exogenous near-infrared (NIR) photon energy into hyperthermia to destroy tumors, the progress of which also known as photothermal therapy, have received broad attention and vigorously developed, especially activable in the NIR II (950–1700 nm) window.[16–19] Depressingly, most of the current PTAs are inorganic nanomaterials characterized by strong rigidity, poor biodegradable, and doping organic substances, which easily result in undesired toxicity to the body.[20–22] In comparison, organic polypyrrole (PPy) that fabricated using safe substrates and green technology possesses good biocompatibility and biosafety, which in the meantime, has comparative NIR absorbance and photothermal conversion efficiency due to its conjugated bond structure and repeating

[a]*Department of Radiation Oncology, The People's Hospital of Guangxi Zhuang Autonomous Region, Nanning 530000, China*
[b]*Department of Joint Surgery and Sports Medicine, The People's Hospital of Guangxi Zhuang Autonomous Region, Nanning 530000, China*
[c]*The First Tumor Department, Maoming People's Hospital, Maoming 525000, China*
[d]*School of Pharmaceutical Sciences, Health Science Center, Shenzhen University, Shenzhen 518000, China*

† Electronic supplementary information (ESI) available: Additional experimental details and data, including TEM image of AuP; hydrodynamic diameter variation of AuP@MnO_2; X-ray energy dispersive spectroscopy (EDS) of AuP@MnO_2; linear relationship between concentration and absorbance of AuP@MnO_2 solutions at 808 and 1064 nm; GSH depletion profile by AuP@MnO_2 with concentrations of 0 μg mL^{-1}, 12.5 μg mL^{-1}, 25 μg mL^{-1}, 50 μg mL^{-1}, and 100 μg mL^{-1}, the photograph of the solutions after 60 min of co-incubation; relative cell viabilities of 4T1 cells cultured with pure medium, AuP, or AuP@MnO_2 and irradiated by a 1064 nm laser (1.0 W cm^{-2}, 5 min). See DOI: https://doi.org/10.1039/d3ra04779b

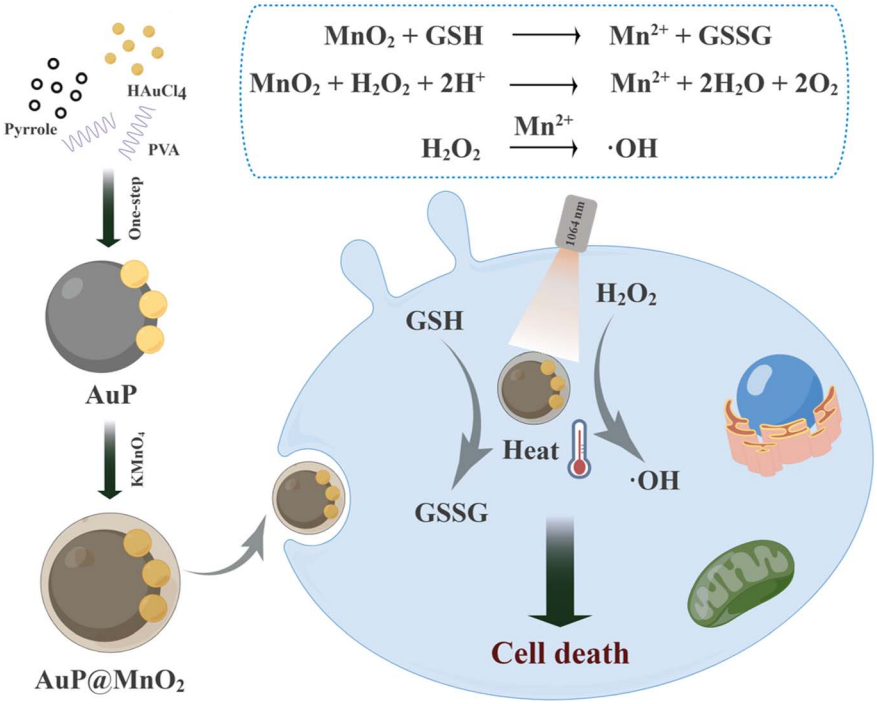

Scheme 1 Schematic illustration of the synthesis of AuP@MnO2 and their application for cancer synergistic therapy.

pyrrole units with delocalized π-electron system, making it serve as an excellent PTAs in cancer treatment.[23–25] Unfortunately, unlike another commonly used organic polymer porous organic frameworks that included cavity hole structures, the development of PPy-based catalysts is still in the infancy stage, with only a limited number of Fe^{2+} or Cu^{+}-triggered Fenton catalysis examples.[26–28] Therefore, it is of great interest to integrate PPy with catalysts containing Mn^{2+} into one nanomedicine to amplify catalytic reaction under photothermal effect.

Generally, PPy is obtained by oxidative polymerization of pyrrole monomer in the simultaneous presence of stabilizers, protic acid, and oxidants. To develop functionalized PPy rather than PPy-based complex, oxidants with therapeutic properties like ferric trichloride, copper dichloride, and ammonium persulfate are employed to initiate the pyrrole polymerization while being present in the PPy nanostructure in ionic form through electrostatic and coordination interactions.[29–32] In the complex physiological environments, however, the doped ions are unstable and easily detached, which increases the risk of side effects on the body.[33,34] As is known, tetrachloroauric acid trihydrate, that has been widely reduced to prepare Au nanoparticles, is a strong oxidant and a protic acid donor that theoretically meets the requirements for initiating pyrrole oxidative polymerization.[35–37] So far, it is still wilderness to directly employ tetrachloroauric acid trihydrate to initiate polymerization, solely limiting to post-modification of PPy on the pre-synthesized seed materials, such as precipitation of tetrachloroauric acid trihydrate on the PPy surface by reduction.

Herein, an asymmetric Au@PPy nanostructure (AuP) was fabricated by one-step tetrachloroauric acid trihydrate-triggered oxidative polymerization of pyrrole without the additional addition of protic acid, in which tetrachloroauric acid trihydrate not only oxidized pyrrole monomers to initial chain polymerization but also provided protic acid to accelerate polymerization efficiency, and meanwhile, itself was reduced to Au nanoparticles within 15 min of polymerization process (Scheme 1). By reducing potassium permanganate on the AuP surface, the prepared core–shell AuP@MnO_2 with good monodispersity and biocompatibility was capable of transforming GSH into GSSG and further catalyzing intracellular H_2O_2 to virulent $^{\cdot}OH$ by MnO_2-mediated Fenton-like reaction in tumor cells, causing oxidative stress damage. Under laser irradiation, AuP@MnO_2 elevated the temperature of the tumor site by AuP-mediated photothermal conversion, which burned the tumor cells while also enhancing the above oxidative damage. In general, this work not only presented a novel tetrachloroauric acid trihydrate-triggered oxidative polymerization method but also promoted the development of nanocatalytic medicine based on polypyrrole.

2. Materials and methods

2.1. Materials and chemicals

All reagents in this study were directly purchased from the manufacturers without further purification. Tetrachloroauric acid trihydrate ($HAuCl_4 \cdot 3H_2O$), methylene blue (MB), and 5,5′-dithiobis (2-nitrobenzoic acid) (DTNB) were purchased from Sigma-Aldrich. Polyvinyl alcohol (PVA, 87–89% alcoholysis degree), pyrrole (99%), sodium bicarbonate ($NaHCO_3$, 99.7%), and glutathione were obtained from Aladdin (Shanghai, China). Potassium permanganate ($KMnO_4$) was provided by Sinopharm Chemical Reagent Co., Ltd. (Guangzhou, China). Dulbecco's modified

eagle's medium (DMEM), fetal bovine serum, and trypsin–EDTA were obtained from Gibco-BRL (Burlington, ON, Canada).

2.2. Synthesis of AuP

10 mL of deionized water and 50 mg of polyvinyl alcohol were added into a 50 mL single-bottom flask, and gently stirred at 90 °C for 1 h. After cooling naturally to room temperature, 5 mL of tetrachloroauric acid trihydrate (10 mM) was added dropwise and stirred continuously for 1 h. Then 200 μL of pyrrole monomer was injected and reacted for 15 min. The resulting AuP was collected and purified by three times of centrifugation (20 000 rpm, 20 min).

2.3. Synthesis of AuP@MnO_2

Under gentle stirring, 25 mL of potassium permanganate aqueous solution (200 μg mL^{-1}) was added dropwise to the solution containing AuP. Then, the mixture was stirred vigorously at 40 °C for 1 h. The resulting AuP@MnO_2 was centrifuged at 15 000 rpm for 10 min and washed three times with deionized water.

2.4. Characterization of nanoparticles

Transmission electron microscopy (TEM) images were acquired on a JEM-2100UHR microscope (JEOL, Japan) to characterize the morphology. X-Ray photoelectron spectroscopy (XPS, ESCALAB 250Xi, Japan) and Fourier transform infrared spectrophotometer spectrum (FTIR, Nexus 470, Nicolet, Madison, WI, USA) were applied to analyze the chemical compositions of AuP or AuP@MnO_2. X-Ray diffraction (XRD, Bruker D8, Germany) was performed to analyze the crystal structure of AuP and AuP@MnO_2. UV-vis-NIR spectrum was investigated by using an Infinite M200 PRO spectrophotometer. The hydrodynamic particle size and zeta potential of AuP or AuP@MnO_2 were monitored by dynamic light scattering (DLS, 15 mW laser, 676 nm incident beam; Brookhaven Instruments Corporation). The scheme illustration was drawn by Figdraw.

2.5. Photothermal performance

To systematically evaluate the photothermal performance of Au@MnO_2, Au@MnO_2 at different concentrations (0, 25, 50, 100, and 200 μg mL^{-1}) was treated with 808 or 1064 nm laser at different power densities (0.5, 1.0, 1.5, and 2.0 W cm^{-2}). Simultaneously, an infrared thermal camera (TI100 IR camera FLK-TI100 9HZ, FLUKE) was used to monitor and record the entire temperature changes. Pure water was irradiated in the same way as a control. To further test photothermal stability, Au@MnO_2 aqueous solution (100 μg mL^{-1}) was irradiated by 808 or 1064 nm laser with the same power density of 1.0 W cm^{-2} and repeated for five cycles, each cycle consisting of 360 s of irradiation and 540 s of shutdown.

2.6. *In vitro* GSH depletion

The depletion of GSH was monitored by UV-vis-NIR spectroscopy. Different concentrations of AuP@MnO_2 nanoparticles (0, 12.5, 25, 50, and 100 μg mL^{-1}) were mixed with GSH (1 mM) solution at 37 °C. At different time points (0, 10, 20, 30, 40, 50, and 60 min), the solutions were removed and mixed with 5,5′-dithiobis-(2-nitrobenzoic acid) (DTNB) (10 mg mL^{-1}), and then the UV-vis-NIR spectroscopy was applied to detect the absorbance of the above suspension.

2.7. *In vitro* Fenton-like activity

50 μg mL^{-1} of AuP@MnO_2 was dispersed in $NaHCO_3$ (25 mM) buffer solution containing GSH (0 or 1 mM) at pH 6.5 and shaken overnight at 37 °C. No-AuP@MnO_2 treatment was used as a control. For the group requiring laser irradiation, the mixture was irradiated with a 1064 nm laser (1.0 W cm^{-2}) for 5 min. After centrifugation, H_2O_2 (10 mM) and MB (10 μg mL^{-1}) were added to the supernatant and measured by UV-vis-NIR spectrophotometer.

2.8. Hemolysis assay

The biosafety of AuP@MnO_2 was firstly evaluated by hemocompatibility testing. Briefly, the red blood cells were obtained by centrifuging fresh mouse blood (4000 rpm, 5 min) and washing several times with PBS (pH 7.4). Afterwards, 300 μL of 8% red blood cells (v/v) were mixed with 700 μL of deionized water (as a positive control group), PBS (as a negative control group), or AuP@MnO_2 dissolved in PBS at different concentrations (6.25, 12.5, 25, 50, 100, 200, and 400 μg mL^{-1}) for 3 h at 37 °C. Ultimately, the samples were centrifuged and measured by UV-vis-NIR spectroscopy and optical microscope.

2.9. Cell cytotoxicity

The *in vitro* cytotoxicity of AuP@MnO_2 to cells was assessed by the standard Cell Counting Kit-8 (CCK-8) assay. Human umbilical vein endothelial cells (HUVEC cells) anf mouse breast cancer cells (4T1 cells) were purchased from the American Type Culture Collection (ATCC). Briefly, human umbilical vein endothelial cells (HUVEC cells) or mouse breast cancer cells (4T1 cells) were seeded in 96-well plates (5000 cells per well) and cultured for 24 h. After washing with PBS, cells were cultured in pure DMEM or DMEM containing AuP@MnO_2 at concentrations of 0, 25, 50, 75, and 100 μg mL^{-1}. After 24 h of incubation, cell viability assay was conducted according to the standard protocol of CCK-8 to detect the relative cell viability by using the SpectraMax M2 plate reader (Molecular Devices, CA, USA).

To evaluate the *in vitro* photo-cytotoxicity of AuP@MnO_2, 4T1 cancer cells (5000 cells per well) were co-cultured with various concentrations (0, 25, 50, 75, and 100 μg mL^{-1}) of AuP@MnO_2 for 6 h. Afterward, the cells were irradiated with 1064 nm laser (1.0 W cm^{-2}) for 5 min and incubated for another 24 h. After that, standard CCK-8 assay was applied to evaluate the cell viabilities. To further compare the photo-cytotoxicity of AuP and AuP@MnO_2, 4T1 cells (5000 cells per well) were co-cultured with pure medium, AuP or AuP@MnO_2 (the equal Au concentration: 9 μg mL^{-1}) and irradiated with 1064 nm laser (1.0 W cm^{-2}) for 5 min.

2.10. Intracellular ˙OH generation

4T1 cells were seeded in confocal dish (2.5×10^5 cells per dish) and cultured overnight. Then cells were treated with pure DMEM or DMEM containing AuP@MnO_2 (50 μg mL^{-1}). After 12 h of incubation, the medium was replaced with DMEM containing 2′,7′-dichlorofluorescin diacetateb (DCFH-DA, 20 μM) and incubated for 30 min, after which the cells in the laser groups were exposed to 1064 nm laser irradiation (1 W cm^{-2}) for 5 min. Then, cells were washed three times with PBS, treated with 4% paraformaldehyde, and stained with DAPI for Confocal Laser Scanning Microscope (CLSM, FV3000, Olympus, Japan) observation.

2.11. Statistical analysis

All statistical analyses were used GraphPad Prism. The results of statistical analysis were presented as mean ± SD. Statistical significance was calculated by one-way ANOVA analysis. The statistical significance was defined as $*p < 0.05$; $**p < 0.01$; $***p < 0.001$.

3. Results and discussion

Asymmetric AuP nanoparticles were synthesized by a one-step tetrachloroauric acid trihydrate-initiated combined chemical oxidation and reduction reaction using polyvinyl alcohol as a stabilizer, where the nanoparticles had a monodispersed structure with a TEM size of around 55 nm (Fig. S1†). The X-ray diffraction (XRD) pattern was used to analyze the crystalline structure of AuP and AuP@MnO_2. As shown in Fig. 1D, both AuP and AuP@MnO_2 revealed cubic Au diffraction peaks (JCPDS 04-0784) at 38.2, 44.4, 64.6, 77.5, and 81.7 °C, indicating that tetrachloroauric acid trihydrate was successfully reduced to Au nanoparticles and the subsequent MnO_2 coating procedure had little effect on the crystalline structure of AuP core. After that, the chemical compositions of AuP and AuP@MnO_2 were confirmed by the Fourier transform infrared (FT-IR) spectra (Fig. 1E). The characteristic peaks that appeared at 3430, 1542, and 1170 cm^{-1} in AuP belonged to the stretching vibrations of N–H, C=C, and C–C in the traditional polypyrrole framework, respectively, suggesting the presence of the chemical structure of polypyrrole in AuP. Meanwhile, relative to the spectra of AuP, the new broad peak at 400–500 cm^{-1} in AuP@MnO_2 was assigned to the stretching vibration of Mn–O, demonstrating the successful coating of MnO_2 shell.[38,39]

By reducing potassium permanganate on the AuP surface, the prepared core–shell AuP@MnO_2 exhibited a analogous morphology and TEM size to the AuP described above (Fig. 1A). For dynamic light scattering measurement, however, the particle size of AuP@MnO_2 increased from ~134 to ~186 nm with a corresponding decrease in surface potential from +8.32 eV to −33.97 eV compared to AuP, confirming the effective encapsulation of the MnO_2 shell (Fig. 1B and C). Moreover,

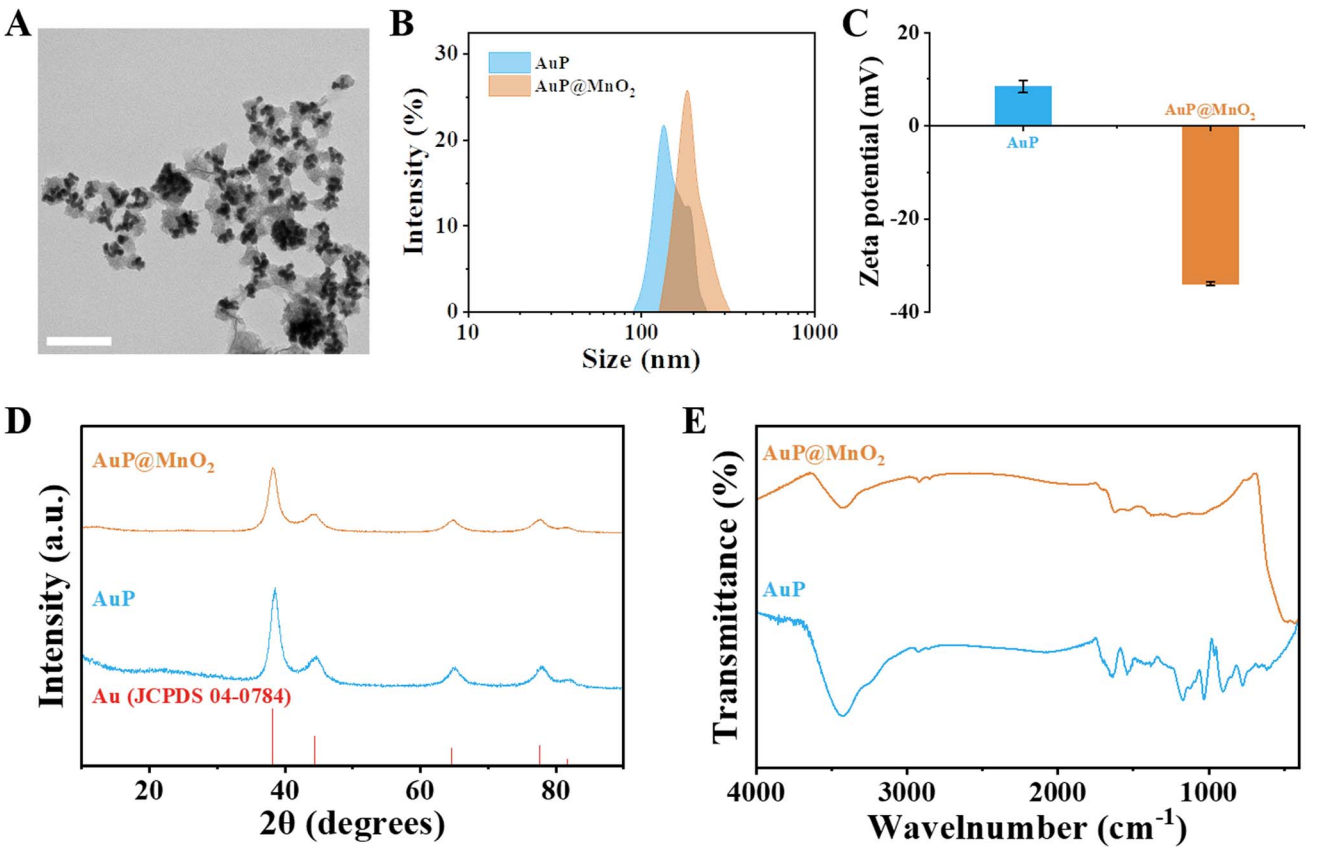

Fig. 1 (A) TEM image of AuP@MnO_2, scale bar: 100 nm. (B) The size distribution and (C) zeta potentials of AuP and AuP@MnO_2. (D) XRD and (E) FTIR spectra of AuP and AuP@MnO_2.

AuP@MnO_2 exhibited good colloidal stability in phosphate buffer for 96 h, with just a ~33 nm size increase compared to 0 h (Fig. S2†). To further evaluate the chemical composition and state of AuP@MnO_2, elemental mapping images and X-ray photoelectron spectroscopy (XPS) spectra were carried out. As shown in Fig. 2C, the uniform and overlapping distribution of Au, Mn, C, N, and O elements in AuP@MnO_2 demonstrated the successful fabrication of core–shell AuP@MnO_2. The energy dispersive X-ray (EDX) spectrum further confirmed the coexistence of Mn and Au elements in the as-prepared AuP@MnO_2 (Fig. S3†). In addition, an emerging Mn 2p peak in the AuP@MnO_2 group was observed in comparison to the XPS spectra of AuP, reconfirming the coating of MnO_2 shell (Fig. 2A). Specifically, from the high-resolution XPS spectrum of Mn 2p, the characteristic peaks at 642.3 and 653.9 eV severally belonged to Mn $2p_{3/2}$ and Mn $2p_{1/2}$, indicating the existence of Mn in its tetravalent form (Fig. 2B). Furthermore, two peaks at 83.4 and 87.1 eV ascribing to Au $4f_{7/2}$ and Au $4f_{5/2}$, respectively, were observed in the high-resolution XPS spectrum of Au 4f, demonstrating the presence of Au in its nonvalent form.

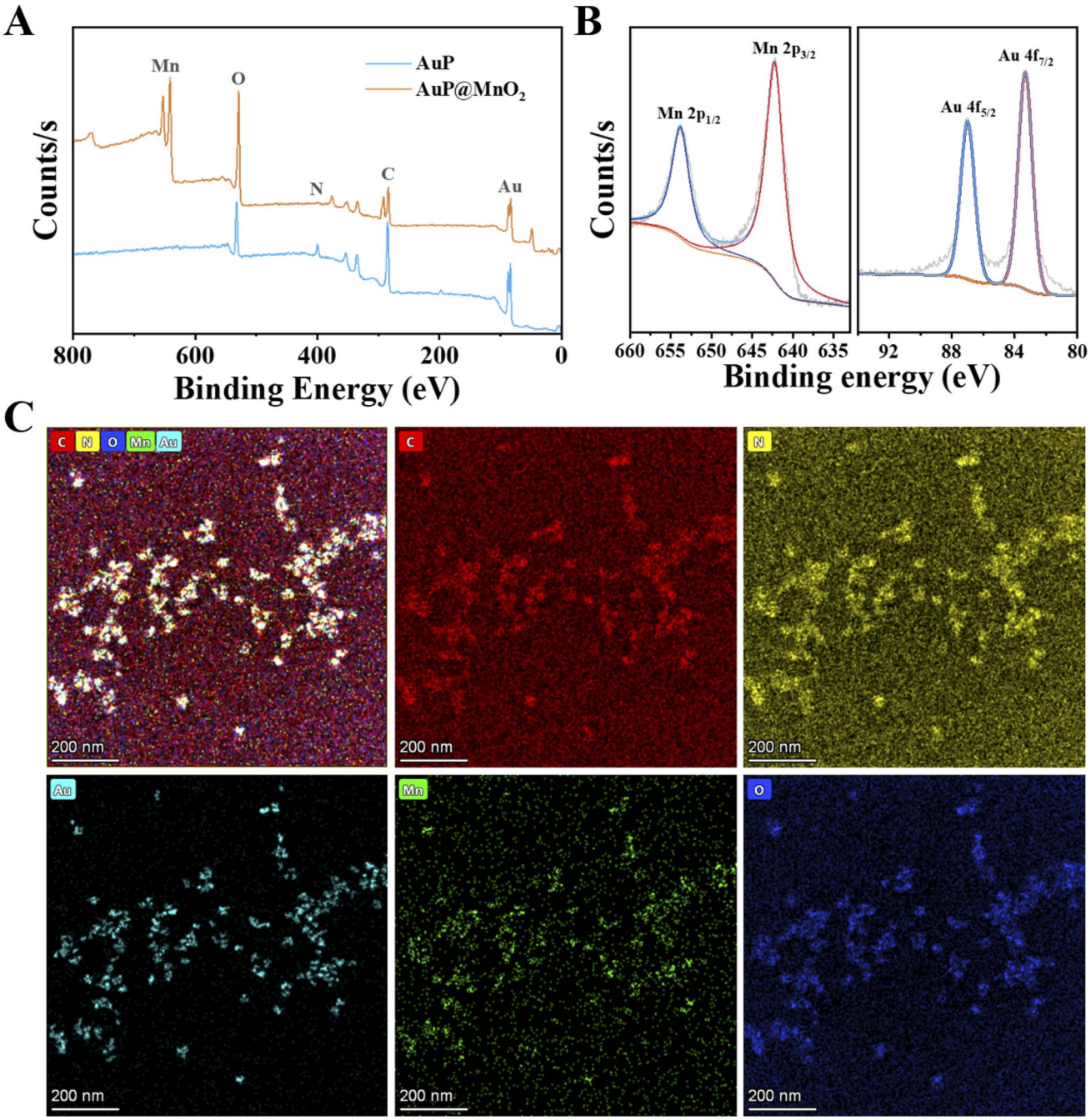

Fig. 2 (A) XPS spectra of AuP and AuP@MnO_2. (B) The corresponding high-resolution XPS spectra of Mn 2p and Au 4f in AuP@MnO_2 group. (C) Elemental mapping images of AuP@MnO_2.

Subsequently, the optical absorbance and photothermal properties of AuP@MnO_2 aqueous solution were examined. As displayed in Fig. 3G, AuP@MnO_2 showed a board absorbance ranging from vis to NIR bio-window. Besides, the optical absorbance of AuP@MnO_2 at 808 or 1064 nm wavelength increased linearly with increasing concentrations (6.25, 12.5, 25, 50, and 100 μg mL^{-1}), indicating the potential of photothermal conversion of AuP@MnO_2 under 808 or 1064 nm laser irradiation (Fig. S4†). Then, the photothermal performance of AuP@MnO_2 was further assessed by monitoring the temperature variation of AuP@MnO_2 with various concentrations (25, 50, 100, and 200 μg mL^{-1}) under an 808 or 1064 nm laser at various power densities (0.5, 1.0, 1.5, and 2.0 W cm^{-2}). No matter whether AuP@MnO_2 was exposed to 808 or 1064 nm laser irradiation at the same power density (1.0 W cm^{-2}), it was evident that the temperature change (ΔT) was time- and concentration-dependent (Fig. 3A and D). After receiving 300 s of 808 or 1064 nm laser irradiation, the temperature of AuP@MnO_2 at a relatively low concentration (100 μg mL^{-1}) could reach 56.9 and 59.6 °C, respectively. In contrast, there was no significant temperature increase for pure water irradiated under the same conditions, indicating that AuP@MnO_2 serving as good PTAs could efficiently and rapidly convert NIR I/II light into thermal energy. We further examined the photothermal performance of AuP@MnO_2 with a concentration of 100 μg mL^{-1} at different power densities of 808 or 1064 nm laser irradiation, and the results revealed a strong power-dependent photothermal effect (Fig. 3B and E). Afterwards, we evaluated the photothermal stability of AuP@MnO_2 suspension by five cycles of laser irradiation and cooling, and the results demonstrated that they maintained remarkable photothermal stability (Fig. 3C and F).

Benefitting from the presence of the MnO_2 shell in AuP@MnO_2 as described above, we initially assessed the ability of AuP@MnO_2 to deplete GSH by utilizing the particular probe 5,5-dithiobis-(2-nitrobenzoic acid) (DTNB), which can react with

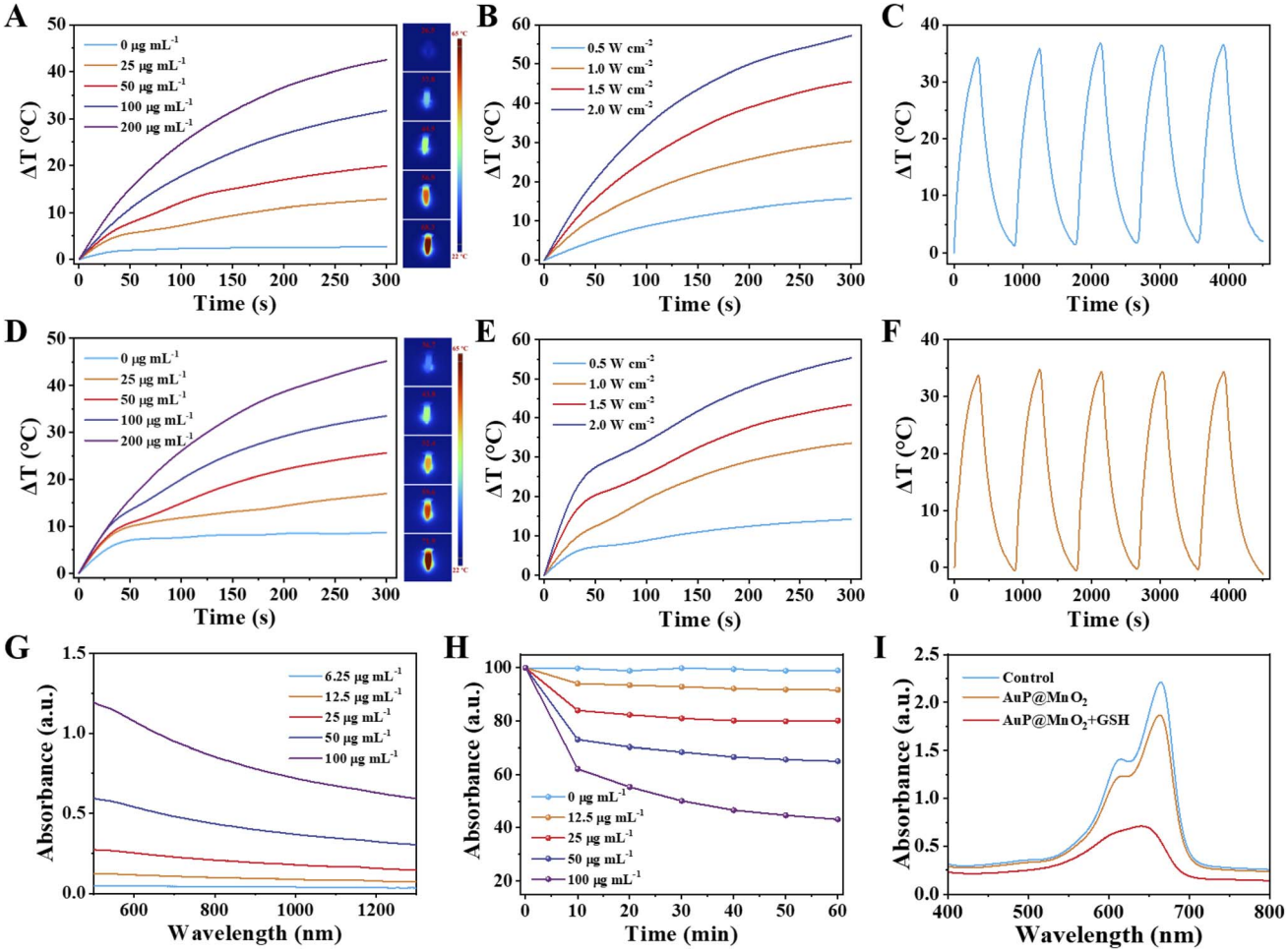

Fig. 3 Temperature changes of AuP@MnO_2 under irradiation for 300 s by an (A) 808 or (D) 1064 nm laser. Temperature changes of AuP@MnO_2 under irradiation for 300 s by an (B) 808 or (E) 1064 nm laser at the different power density (0.5, 1.0, 1.5, and 2.0 W cm^{-2}). Photothermal stability of AuP@MnO_2 solution for five laser on/off cycles under the irradiation of (C) 808 or (F) 1064 nm laser (1.0 W cm^{-2}). (G) UV-vis-NIR absorbance spectra of AuP@MnO_2 solutions at varied concentrations (6.25, 12.5, 25, 50, and 100 μg mL^{-1}). (H) The degradation of GSH caused by AuP@MnO_2 with different concentrations (0, 12.5, 25, 50, and 100 μg mL^{-1}). (I) The degradation of MB caused by different treatments.

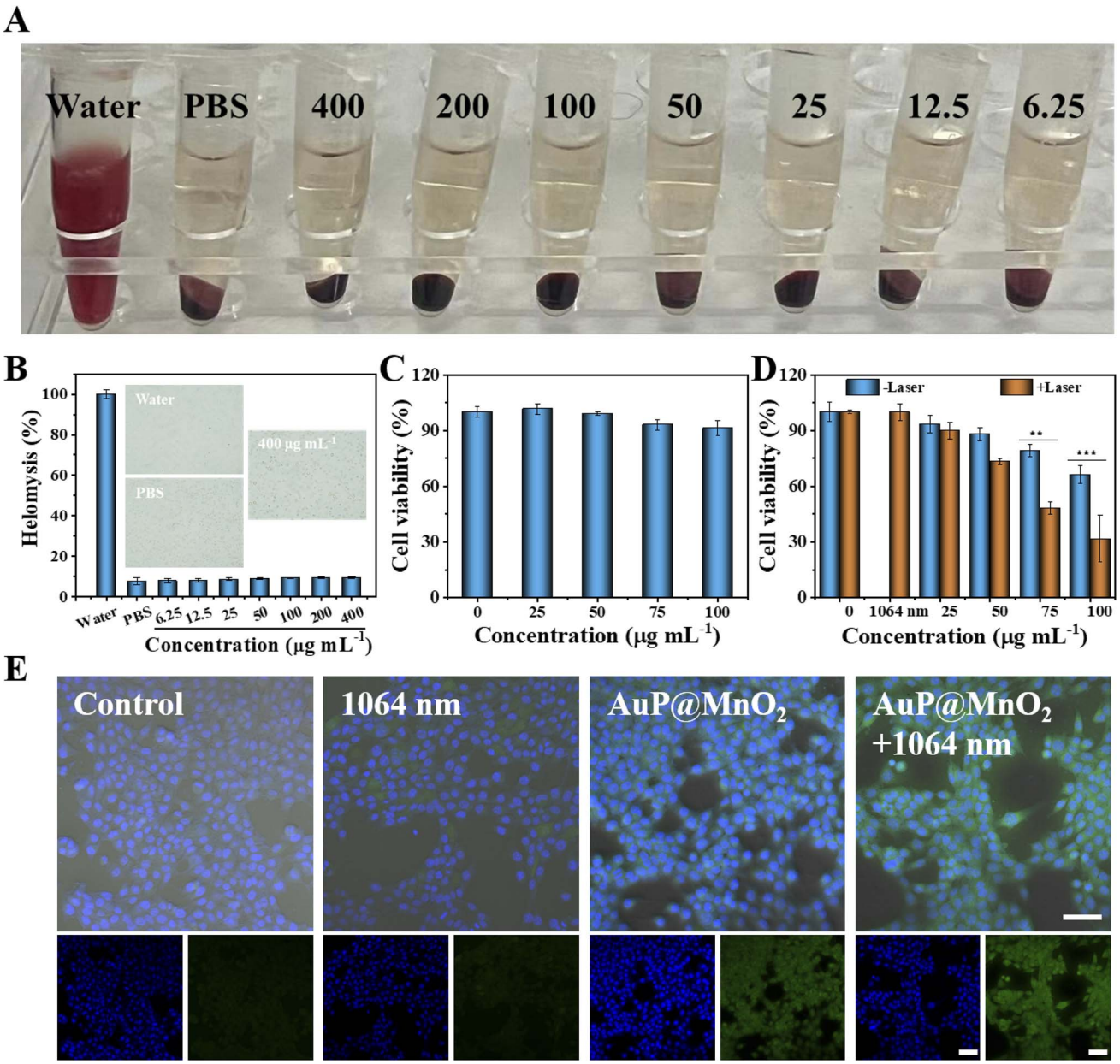

Fig. 4 (A and B) Hemolysis assay of red blood cells after incubating with water, PBS, and AuP@MnO_2 dispersed in PBS at various concentrations. Inset: microscope pictures of different samples at the end of the experiment. (C) Relative cell viabilities of HUVEC and 4T1 cells after incubating with various concentrations of AuP@MnO_2 (0, 25, 50, 75, and 100 μg mL^{-1}) for 24 h. (D) Relative cell viabilities of 4T1 cells after incubating with AuP@MnO_2 and irradiated by a 1064 nm laser (1.0 W cm^{-2}, 5 min). (E) CLSM images of intracellular ·OH generation in 4T1 cells after different treatments, scale bar: 100 μm. Data represent means ± SD ($n = 3$). Statistical significance was calculated by one-way ANOVA analysis. *p <0 .05; **p< 0 .01; ***p< 0 .001.

the sulfhydryl group of GSH to produce yellow 5-thio-2-nitrobenzoic acid with a maximum absorption peak at ~412 nm.[40] A rapid and sustained concentration-dependent consumption of GSH was observed (Fig. 3H and S5†), which was attributed to the redox reaction between MnO_2 and GSH to generate Mn^{2+} and GSSG, demonstrating the considerable decrease in oxidation resistance property after AuP@MnO_2 treatment. To confirm the Fenton-like activity of AuP@MnO_2, methylene blue (MB) was used as a probe to detect hydroxyl radicals (˙OH) production in the bicarbonate buffer. Because of the breakdown of AuP@MnO_2 into Mn^{2+} at the acidic pH and the subsequent Fenton-like reaction between Mn^{2+} and H_2O_2, as seen in Fig. 3I, the absorbance of MB was slightly reduced after being incubated with AuP@MnO_2 and H_2O_2. Remarkably, MB had notably degraded when treated with AuP@MnO_2 and H_2O_2 under reducing conditions, revealing that a large amount of MnO_2 existing in the framework of AuP@MnO_2 would be reduced to Mn^{2+} by GSH and subsequently propelled Mn^{2+}-mediated Fenton-like reaction for generating ˙OH. In addition,

a single 1064 nm laser irradiation further increased Fenton-like reaction and $^{\bullet}OH$ generation.

Encouraged by the good photothermal and catalytic properties of AuP@MnO_2, the combined antitumor effect of AuP@MnO_2 was further studied at the cellular level with and without laser irradiation. The initial goal of the AuP@MnO_2 hemolysis experiment was to assess the potential for biomedical applications. The outcomes showed that even at the highest concentration of 400 μg mL^{-1}, the hemolytic activity of AuP@MnO_2 was very low after co-culturing with red blood cells for 3 h (Fig. 4A and B), indicating the high hemocompatibility of AuP@MnO_2. Additionally, no significant cytotoxicity was observed after co-incubating AuP@MnO_2 (0–100 μg mL^{-1}) with normal cell (HUVEC cells) for 24 h (Fig. 4C), indicating the satisfactory biocompatibility of AuP@MnO_2. In contrast, when AuP@MnO_2 was cultured with cancer cell (4T1 cells) for 24 h, cell viability decreased and reached as low as 66.4% at the maximum concentration of 100 μg mL^{-1}, which might be attributed to the acidity and overexpressed H_2O_2 in tumor cells. Interestingly, the viabilities of 4T1 tumor cells decreased noticeably more after receiving AuP@MnO_2 and laser treatment, confirming the good combination anticancer effect of AuP@MnO_2 under 1064 nm laser exposure (Fig. 4D). Meanwhile, under the same Au concentration and light conditions, the AuP@MnO_2 group exhibited a lower cell survival rate than the AuP group, which was attributed to MnO_2-mediated catalytic toxicity (Fig. S6†). In general, the skilful integration of the AuP and MnO_2 components into a single nanomedicine (AuP@MnO_2) was more advantageous for tumor killing than either AuP-mediated photothermotoxicity or Mn^{2+}-mediated Fenton toxicity. Next, we evaluated the catalytic property of AuP@MnO_2 for generating $^{\bullet}OH$ at the cellular level. As shown in Fig. 4E, the green fluorescence signal was rather faint in the 1064 nm laser irradiation group, nevertheless in the AuP@MnO_2 group, the green fluorescence signal was dramatically increased due to Fenton-like catalysis. Notably, the strongest $^{\bullet}OH$ fluorescence signal was observed in cells treated with AuP@MnO_2 plus laser irradiation, which was ascribed to the combined effect of photothermal therapy and catalytic therapy.

4. Conclusion

In summary, an innovative asymmetric AuP nanoparticles was successfully developed by one-step tetrachloroauric acid trihydrate-triggered oxidative polymerization of pyrrole and self-reduction within a reaction time of 15 min, followed by the addition of MnO_2 coating. The obtained AuP@MnO_2 exhibited good biocompatibility and hemocompatibility under normal physiological environment. However, when AuP@MnO_2 was co-cultured with tumor cells, distinct oxidative stress and cytotoxicity could be observed due to the highly efficient redox reaction between AuP@MnO_2 and antioxidant GSH, accompanied by Mn^{2+}-induced Fenton-like reaction. What is more, after 1064 nm laser irradiation, more intense oxidative imbalance and cell death were achieved under the combined effect of photothermal and catalytic therapy. Overall, this work has exploited the enormous potential of AuP@MnO_2 as promising PTAs and catalysts, which also provides a new perspective for the evolution of PPy-based tumor theranostic nanoplatforms.

Author contributions

All authors have given approval to the final version of manuscript.

Conflicts of interest

The authors declare no competing financial interest.

Acknowledgements

This study was supported by the Maoming Science and Technology Plan (No. 2021555) and the High-level Hospital Construction Research Project of Maoming People's Hospital (No. zx2020020).

References

1 B. Yang, Y. Chen and J. Shi, Nanocatalytic medicine, *Adv. Mater.*, 2019, **31**(39), 1901778.
2 P. Chen, X. Zhou, H. Shen, N. M. Andoy, E. Choudhary, K. S. Han, G. Liu and W. Meng, Single-molecule fluorescence imaging of nanocatalytic processes, *Chem. Soc. Rev.*, 2010, **39**, 4560–4570.
3 W. Zeng, H. Zhang, X. Yuan, T. Chen, Z. Pei and X. Ji, Two-dimensional nanomaterial-based catalytic medicine: theories, advanced catalyst and system design, *Adv. Drug Delivery Rev.*, 2022, **184**, 114241.
4 C. Wu, Z. Liu, Z. Chen, D. Xu, L. Chen, H. Lin and J. Shi, A nonferrous ferroptosis-like strategy for antioxidant inhibition-synergized nanocatalytic tumor therapeutics, *Sci. Adv.*, 2021, **7**(39), eabj883.
5 Z. Tang, P. Zhao, H. Wang, Y. Liu and W. Bu, Biomedicine meets fenton chemistry, *Chem. Rev.*, 2021, **121**, 1981–2019.
6 J. Li, M. Chen, D. A. Cullen, S. Hwang, M. Wang, B. Li, K. Liu, S. Karakalos, M. Lucero, H. Zhang, C. Lei, H. Xu, G. E. Sterbinsky, Z. Feng, D. Su, K. L. More, G. Wang, Z. Wang and G. Wu, Atomically dispersed manganese catalysts for oxygen reduction in proton-exchange membrane fuel cells, *Nat. Catal.*, 2018, **1**, 935–945.
7 X. Lu, S. Gao, H. Lin, L. Yu, Y. Han, P. Zhu, W. Bao, H. Yao, Y. Chen and J. Shi, Bioinspired copper single-atom catalysts for tumor parallel catalytic therapy, *Adv. Mater.*, 2020, **32**(36), 2002246.
8 M. Huo, L. Wang, Y. Chen and J. Shi, Tumor-selective catalytic nanomedicine by nanocatalyst delivery, *Nat. Commun.*, 2017, **8**(1), 357.
9 H. Lin, Y. Chen and J. Shi, Nanoparticle-triggered *in situ* catalytic chemical reactions for tumour-specific therapy, *Chem. Soc. Rev.*, 2018, **47**, 1938–1958.
10 Z. Tang, Y. Liu, M. He and W. Bu, Chemodynamic therapy: tumour microenvironment-mediated fenton and fenton-like reactions, *Angew. Chem., Int. Ed.*, 2019, **58**, 946–956.

11 Y. Nie, W. Zhang, W. Xiao, W. Zeng, T. Chen, W. Huang, X. Wu, Y. Kang, J. Dong, W. Luo and X. Ji, Novel biodegradable two-dimensional vanadene augmented photoelectro-fenton process for cancer catalytic therapy, *Biomaterials*, 2022, **289**, 121791.
12 J. D. Rabinowitz and E. White, Autophagy and metabolism, *Science*, 2010, **330**, 1344–1348.
13 X. Cheng, H. D. Xu, H. H. Ran, G. Liang and F. G. Wu, Glutathione-depleting nanomedicines for synergistic cancer therapy, *ACS Nano*, 2021, **15**, 8039–8068.
14 X. Wang, X. Zhong, Z. Liu and L. Cheng, Recent progress of chemodynamic therapy-induced combination cancer therapy, *Nano Today*, 2020, **35**, 100946.
15 Y. Zhou, S. Fan, L. Feng, X. Huang and X. Chen, Manipulating intratumoral fenton chemistry for enhanced chemodynamic and chemodynamic-synergized multimodal therapy, *Adv. Mater.*, 2021, **33**(48), 2104223.
16 X. Li, J. F. Lovell, J. Yoon and X. Chen, Clinical development and potential of photothermal and photodynamic therapies for cancer, *Nat. Rev. Clin. Oncol.*, 2020, **17**(11), 657–674.
17 J. Kim, J. Kim, C. Jeong and W. J. Kim, Synergistic nanomedicine by combined gene and photothermal therapy, *Adv. Drug Delivery Rev.*, 2016, **98**, 99–112.
18 C. Xu and K. Pu, Second near-infrared photothermal materials for combinational nanotheranostics, *Chem. Soc. Rev.*, 2021, **50**, 1111–1137.
19 W. Zeng, H. Zhang, Y. Deng, A. Jiang, X. Bao, M. Guo, Z. Li, M. Wu, X. Ji, X. Zeng and L. Mei, Dual-response oxygen-generating MnO_2 nanoparticles with polydopamine modification for combined photothermal-photodynamic therapy, *Chem. Eng. J.*, 2020, **389**, 124494.
20 R. R. Arvizo, S. Bhattacharyya, R. A. Kudgus, K. Giri, R. Bhattacharya and P. Mukherjee, Intrinsic therapeutic applications of noble metal nanoparticles: past, present and future, *Chem. Soc. Rev.*, 2012, **41**, 2943–2970.
21 X. Wang, X. Zhong, J. Li, Z. Liu and L. Cheng, Inorganic nanomaterials with rapid clearance for biomedical applications, *Chem. Soc. Rev.*, 2021, **50**, 8669–8742.
22 H. Zhang, W. Zeng, C. Pan, L. Feng, M. Ou, X. Zeng, X. Liang, M. Wu, X. Ji and L. Mei, SnTe@MnO_2-SP nanosheet-based intelligent nanoplatform for second near-infrared light-mediated cancer theranostics, *Adv. Funct. Mater.*, 2019, **29**(37), 1903791.
23 T. Chen, W. Zeng, Y. Liu, M. Yu, C. Huang, Z. Shi, C. Lin, J. Tang, L. Mei and M. Wu, Cu-doped polypyrrole with multi-catalytic activities for sono-enhanced nanocatalytic tumor therapy, *Small*, 2022, **18**(29), 2202964.
24 Y. Wang, W. Zeng, H. Liang, X. Wu, H. Li, T. Chen, M. Yang, X. Wang, W. Li, F. Zhang, Q. Li, F. Ye, J. Guan and L. Mei, Targeted wolfram-doped polypyrrole for photonic hyperthermia-synergized radiotherapy, *ACS Appl. Mater. Interfaces*, 2022, **14**(45), 50557–50568.
25 X. Song, Q. Chen and Z. Liu, Recent advances in the development of organic photothermal nano-agents, *Nano Res.*, 2015, **8**, 340–354.
26 W. Zeng, M. Yu, T. Chen, Y. Liu, Y. Yi, C. Huang, J. Tang, H. Li, M. Ou, T. Wang, M. Wu and L. Mei, Polypyrrole nanoenzymes as tumor microenvironment modulators to reprogram macrophage and potentiate immunotherapy, *Adv. Sci.*, 2022, **9**(23), 2201703.
27 W. Feng, X. Han, R. Wang, X. Gao, P. Hu, W. Yue, Y. Chen and J. Shi, Nanocatalysts-augmented and photothermal-enhanced tumor-specific sequential nanocatalytic therapy in both NIR-I and NIR-II biowindows, *Adv. Mater.*, 2019, **31**(5), 1805919.
28 J. Liang, Y. Huang and R. Cao, Metal–organic frameworks and porous organic polymers for sustainable fixation of carbon dioxide into cyclic carbonates, *Coord. Chem. Rev.*, 2019, **378**, 32–65.
29 A. Malinauskas, Chemical deposition of conducting polymers, *Polymer*, 2001, **42**, 3957–3972.
30 M. Amaike and T. Iihama, Chemical polymerization of pyrrole with disulfide structure and the application to lithium secondary batteries, *Synth. Met.*, 2006, **156**, 239–243.
31 J. Pecher and S. Mecking, Nanoparticles of conjugated polymers, *Chem. Rev.*, 2010, **110**, 6260–6279.
32 W. Zeng, X. Wu, T. Chen, S. Sun, Z. Shi, J. Liu, X. Ji, X. Zeng, J. Guan, L. Mei and M. Wu, Renal-clearable ultrasmall polypyrrole nanoparticles with size-regulated property for second near-infrared light-mediated photothermal therapy, *Adv. Funct. Mater.*, 2021, **31**(15), 2008362.
33 B. Gu and Q. Zhang, Recent advances on functionalized upconversion nanoparticles for detection of small molecules and ions in biosystems, *Adv. Sci.*, 2018, **5**(3), 1700609.
34 C. H. Lu, G. V. Biesold-McGee, Y. Liu, Z. Kang and Z. Lin, Doping and ion substitution in colloidal metal halide perovskite nanocrystals, *Chem. Soc. Rev.*, 2020, **49**, 4953–5007.
35 K. Saha, S. S. Agasti, C. Kim, X. Li and V. M. Rotello, Gold nanoparticles in chemical and biological sensing, *Chem. Rev.*, 2012, **112**, 2739–2779.
36 T. Chen, W. Zeng, C. Tie, M. Yu, H. Hao, Y. Deng, Q. Li, H. Zheng, M. Wu and L. Mei, Engineered gold/black phosphorus nanoplatforms with remodeling tumor microenvironment for sonoactivated catalytic tumor theranostics, *Bioact. Mater.*, 2022, **10**, 515–525.
37 K. Huang, H. Ma, J. Liu, S. Huo, A. Kumar, T. Wei, X. Zhang, S. Jin, Y. Gan, P. C. Wang, S. He, X. Zhang and X. J. Liang, Size-dependent localization and penetration of ultrasmall gold nanoparticles in cancer cells, multicellular spheroids, and tumors *in vivo*, *ACS Nano*, 2012, **6**, 4483–4493.
38 L. Zhang, J. Wang, H. Qiao, F. Liu and Z. Fu, Synthesis of manganese oxides for adsorptive removal of ammonia nitrogen from aqueous solutions, *J. Cleaner Prod.*, 2020, **272**, 123055.
39 G. Tan, Y. Liu and D. Xiao, Preparation of manganese oxides coated porous carbon and its application for lead ion removal, *Carbohydr. Polym.*, 2019, **219**, 306–315.
40 D. Glustarini, I. Dalle-Donne, A. Milzani, P. Fanti and R. Rossi, Analysis of GSH and GSSG after derivatization with *N*-ethylmaleimide, *Nat. Protoc.*, 2013, **8**(9), 1660–1669.